Metascience in Aerospace

https://www.aimspress.com/journal/mina

Metascience in Aerospace, 2(3): 42–67.
DOI:10.3934/mina.2025003
Received: 23 June 2025
Revised: 25 June 2025
Accepted: 31 July 2025
Published: 15 August 2025

Research article

USAT-I attitude control system trade-off studies, stability analysis and simulations

Elián Hanisch[1] **and Pablo Servidia**[2,*]

[1] UIDET SENyT - Electrical Engineering Department, Faculty of Engineering, National University of La Plata, Argentina

[2] CONAE - National Commission of Space Activities, Av. Paseo Colón 751, CABA, Argentina

* **Correspondence:** Email: pservidia@conae.gob.ar; Tel: +541143310074.

Abstract: In this work, a comparison was made between possible detumbling and Sun-pointing attitude controls for the USAT-I 3U CubeSat, considering a magnetic-only control versus a combination between coils and a single reaction wheel. The simulation considered software-in-the-loop simulation using NASA's 42 simulator with ad-hoc control law routines. The result is instrumental in defining the trade-off at the system level, considering the power generation on each case for a class of Sun-synchronous orbits as a function of the orbit local hour. As the satellite orbit is not known in advance, the control must be evaluated along different scenarios, with and without an eclipse, considering a near circular and near polar orbit as typical for LEO launch opportunities. For all these actuator cases the nonlinear system is also time varying and underactuated, hence the stability analysis was made using the averaging theory. This includes a Sun-pointing mode with spin, which makes the mission more feasible under operational constraints. The Sun-pointing error feedback was evaluated using a partial quaternion defined in this context.

Keywords: USAT-I; CubeSat; attitude control; magnetic control; detumbling; Sun-pointing

---

Abbreviations: ACS: Attitude control system; CSS: Coarse Sun sensor; GNSS: Global navigation satellite system; GNSS-RO: Radio occultation using GNSS signals; GNSS-R: Reflectometry using GNSS signals; IMU: Inertial measurement unit; MTB: Magnetic torque bar; LTAN: Local time of ascending node; RAAN: Right ascension of the ascending node; RW: Reaction wheel; TAM: Three-axis magnetometer

1. Introduction

CubeSats have been stabilized in several ways, including passive control [1, 2], magnetic-only actuation [3], gravity gradient and aerodynamic passive control [4], magnetic and aerodynamic control [5], magnetic and gravity gradient control, momentum bias and control moment gyros strategies [6], fluid-dynamic actuation [7], thruster control [8], and the typical three-axis stabilization and trajectory tracking using a set of wheels as main attitude control actuators with complementary coils for detumbling and wheel desaturation [9]. The validation steps of these techniques usually begin with numerical simulations and progressively include hardware in the loop [10].

This paper is based on the trade-off analysis made for the USAT-I, the first CubeSat developed by Argentina's National University of La Plata [11], whose main payload aims to test GNSS technology for Earth observation (see [12]).

As this is a low-budget project, we need to solve the mission pointing needs with reduced cost and complexity, which leads to a fully magnetic control as the first concept. We show that this may not be enough for the mission performance, so we consider as an alternative the addition of one reaction wheel. From the analysis point of view, we notice that the treatment made in [13] (Section 7.4) for an attitude control with magnetorquers considers that three-axis control is locally feasible by replacing one magnetorquer with one wheel. We claim that this is not actually true when the wheel becomes perpendicular to the magnetic field, and provide a solution using the general averaging theory (see [14]). Moreover, we provide this proof for an important practical problem given by the pointing of a certain desired axis (typically the vector normal to the main solar panel) to the Sun in two variants: inertial Sun-pointing and Sun-pointing with spin. To this end, the partial quaternion definition made in [15] is instrumental in representing the pointing error of a single vector instead of a frame.

The objective of this paper is to decide between the possible control laws, sensors, and actuators to use on these modes, and to show the result of the implementation made as a routine to run on NASA's 42 simulator [16, 17]. The analysis uses nonlinear control theory as made also in [18, 19, 20, 21, 22] for this system in nominal conditions and considering failures. Here we put focus on the trade-off between a fully magnetic control and the addition of a single reaction wheel, considering also the axis selection.

In Section 2 we summarize the main features of the USAT-I mission. Section 3 defines the control laws to be evaluated for this mission, including the definition of a quaternion-like vector as the Sun-pointing error, and the associated stability analysis. The description of the implementation using the 42 simulator is made in Section 4, showing extracts from the input files which define the sensors, actuators, spacecraft body, and main simulation parameters; the associated attitude control routines are provided as complementary material. The implementation was straightforward, which emphasizes the benefits of the 42 simulator to model and test the attitude control subsystem. The numerical results are shown and discussed in Section 5, while the conclusions are given in Section 6.

2. USAT-I mission

The USAT-I is the first CubeSat project developed by the National University of La Plata, in Argentina, whose main purpose is to test GNSS techniques for Earth observation [11], such as radio-occultation (GNSS-RO) and reflectometry (GNSS-R) (see [12]). It is a 3U body with fixed solar panels located on two opposite long faces, as shown in Figure 1, with its main parameters given in Table 1.

Table 1. USAT-I main parameters.

Mass	3 kg
Dimensions	10 cm × 10 cm × 30 cm
Moments of inertia	J_{xx} = 0.031 Nms^2, J_{yy} = 0.031 Nms^2, J_{zz} = 0.007 Nms^2

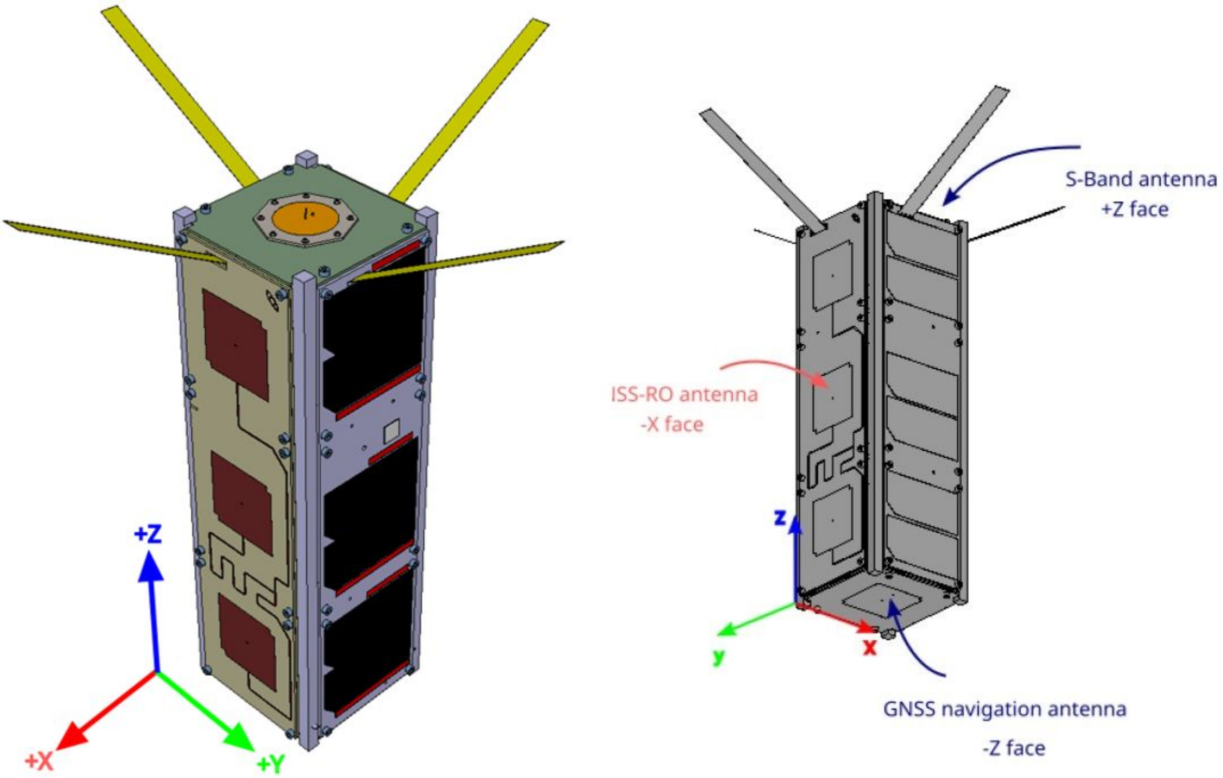

Figure 1. USAT-I body frame definition, with the location of antennas and solar cells.

In order to reduce the cost, the high-cost items such as star trackers, reaction wheels, and GNSS receivers have to be minimized without losing autonomy. Here we seek a simple solution which does not rely on orbit information, does not require three-axis stability, and could operate regardless of the eclipse duration, under mild orbital assumptions, by evaluating the combination between magnetic-only control and the option of one reaction wheel. In fact, although the minimum cost is realized with no wheels, the increased performance (with improved power generation) and robustness determined the selection of three magnetorquers and one wheel. Moreover, the onboard attitude determination is reduced to the partial quaternion using the Sun vector, while the three-axis attitude determination will be implemented off-line to correlate payload observations, using the magnetic vector, the Sun vector, the angular velocity, orbital information, and appropriate models.

The nominal mission concept includes the following attitude control modes and objectives:

- M_1: To reduce the initial angular velocity due to tip-off rates after separation from the launch vehicle.
- M_2: To point one of the (opposite) solar panels to the Sun.
- M_3: Generate a configurable angular velocity around the vector pointing to the Sun.

Mode M_3 is useful to determine different payload antennae-pointing scenarios for the GNSS experiment on a dawn/dusk orbit. The transition between M_1 and M_2 is automatic once the norm of the angular velocity is lower than a threshold. Both transitions between M_2 and M_3 would be commanded by the ground segment, while M_3 may return to M_2 automatically if the power generation were not enough to keep this mode, as shown in Figure 2. The associated sensors and actuators for each mode are activated as follows:

- M_1: Three-Axis Magnetometer (TAM), 3×Gyros, 3×Magnetic Torque Bars (MTB).

- M_2: TAM, 6×Coarse Sun Sensors (CSS), 3×Gyros, 3×MTB, and one optional Reaction Wheel (RW).
- M_3: TAM, 6×CSS, 3×Gyros, 3×MTB, and one RW.

Mode M_2 has a faster response and better performance (and hence more power generation) by adding the wheel, although it is also feasible under full magnetic control. The need of the reaction wheel (RW) and the selection of its axis will be evaluated by analysis and simulations. Moreover, at the current development stage the orbit is not defined, hence the operational constraints of the M_3 mode shall be evaluated at a later stage. Other modes might be considered for science objectives.

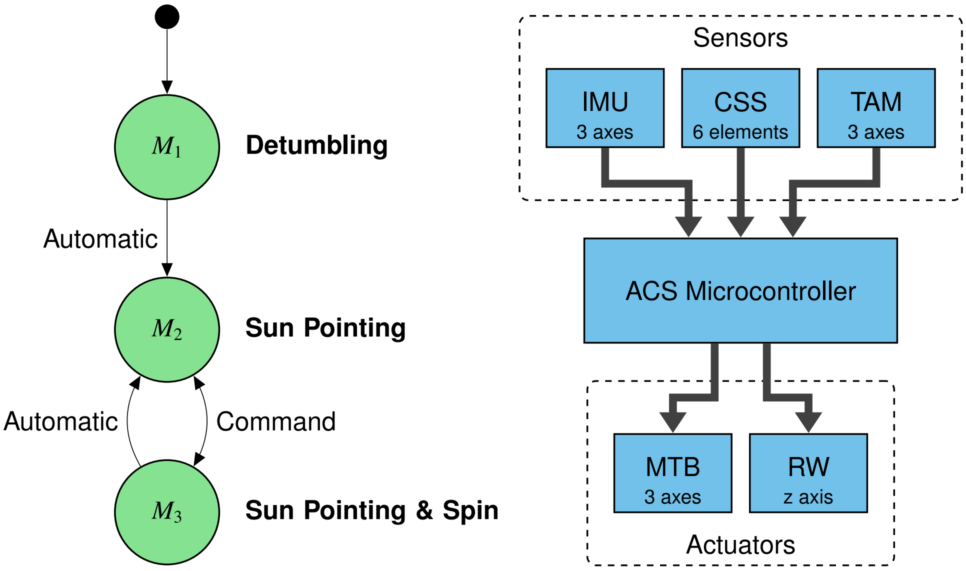

Figure 2. USAT-I ACS modes with the type of transitions, sensors, and actuators.

The control laws are tested first numerically against the 42 simulator, which is the main goal of this research. In a second step, the ACS software is tested with the real serial interfaces against an emulator which translates them into the input/output variables of the 42 simulator. Finally, the routines of the flight software are tested against each hardware in a flat-sat, as shown in Figure 3. The RW and MTB for the X and Y axes are visible at the top, while the Z axis MTB is partially shown below. The Verification and Validation steps will continue including the final satellite integration on functional and environmental testing.

3. Definition of control laws

Here we define the control laws to be evaluated by simulations for the USAT-I attitude control. The main tool is the averaging theory, which has been applied for this problem following the control law introduced by Astolfi and Lovera in [14]. It is not our purpose to show all the details of the proofs, but to provide each control law definition, the associated Lyapunov function, and its derivative, while the details on the validity of the averaging are assumed as in [14]. In particular, the proportional and derivative gains will depend on a scaling variable $\epsilon > 0$, which is justified in the context of the averaging theory for the convergence of true solutions to averaged solutions. The first two subsections give the necessary background on the spacecraft model and magnetic control.

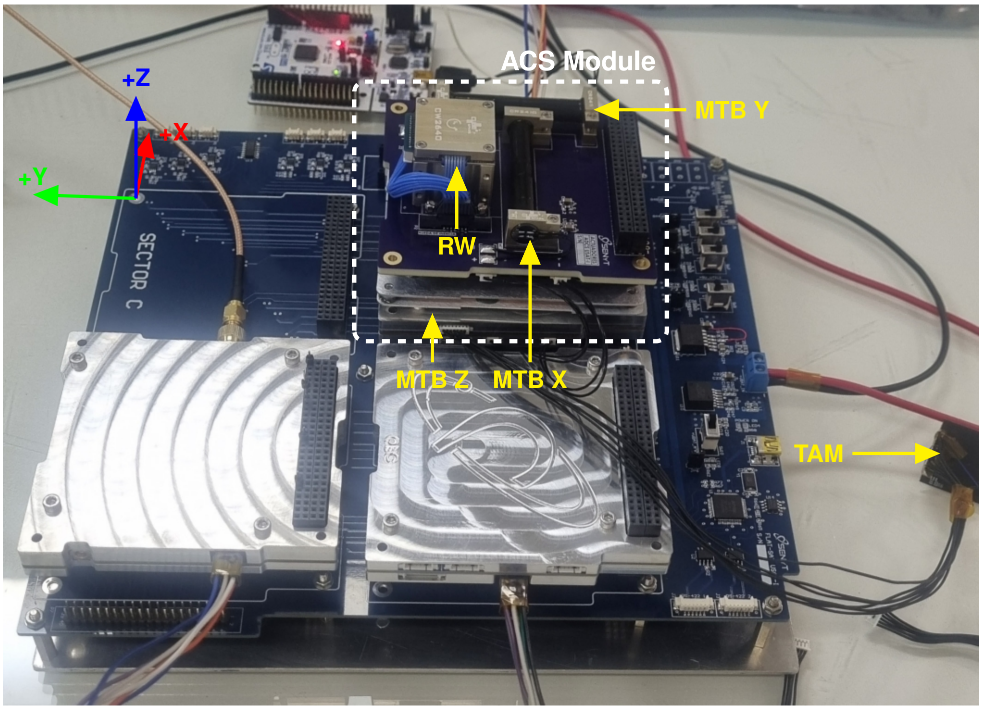

Figure 3. ACS module and the external three-axis magnetometer (TAM) performing functional tests in a FlatSat configuration. A body frame is shown as a reference.

3.1. *Spacecraft model*

We consider the rigid body model for the angular velocity $\underline{\omega} \in \mathbb{R}^3$ and the quaternion $Q = [q_0, \underline{q}^T]^T$, where $q_0 \in \mathbb{R}$ is the scalar part and $\underline{q} \in \mathbb{R}^3$ is the vector part:

$$\left\{ \begin{array}{rcl} \dot{q}_0 & = & -\frac{1}{2}\underline{q}^T\underline{\omega} \\ \dot{\underline{q}} & = & \frac{1}{2}(q_0 I_3 + \underline{q}\times)\underline{\omega} \\ J\dot{\underline{\omega}} & = & -\underline{\omega} \times J\underline{\omega} + T_{mag} \end{array} \right. \tag{3.1}$$

with the identity matrix $I_3 \in \mathbb{R}^{3\times3}$, and $T_{mag} \in \mathbb{R}^3$ is the magnetic control torque to be defined. When one reaction wheel is installed, an additional torque appears in the dynamic equation:

$$J\dot{\underline{\omega}} \;=\; -\underline{\omega} \times (J\underline{\omega} + H_w\underline{k}_w) + T_{mag} + T_w\underline{k}_w \tag{3.2}$$

where $\underline{k}_w$ is the axis of the wheel, $T_w \in \mathbb{R}$ is the torque, and $H_w = J_w\Omega_w$ is its angular momentum associated to a wheel's inertia J_w with speed Ω_w. The term T_d is the drag term of the wheel that is defined as a function of H_w. The dynamic equation of the wheel can be approximated as $\dot{H}_w = -T_w + T_d(H_w)$.

For the detumbling analysis, we will consider $H_w = T_w = 0$. For Sun-pointing, a partial quaternion (as defined in [15]) is considered to measure only the angle between a certain solar panel normal vector and the Sun in the body frame $Q_s = [q_{0s}, \underline{q}_s^T]^T$. Without loss of generality we assume that the Sun objective is one canonical axis, so $(\underline{q}_s)_p = 0$ for a given pointing axis[*] $p \in \{1, 2, 3\}$. Finally, let $\underline{\omega}_s$ be such that $\dot{q}_{0s} = -\frac{1}{2}\underline{q}_s^T\underline{\omega}_s$ with $(\underline{\omega}_s)_p = 0$ and $(\underline{\omega}_s)_i = (\underline{\omega})_i$ for $i \neq p$.

---

[*] For any vector $\underline{x}$, the $i-$th component is $(\underline{x})_i$.

3.2. Magnetic moment and magnetic torque

The magnetic control is underactuated due to the fact that it is only possible to make torque in the two-dimensional subspace normal to the magnetic vector $\underline{b}_b \in \mathbb{R}^3$ in the body frame. For a desired torque $\underline{u} \in \mathbb{R}^3$, the actual magnetic torque T_{mag} is given as [14, 18, 19, 20]:

$$T_{mag} = \Gamma \underline{u} \quad \text{where} \quad \Gamma \triangleq \left[-\frac{\underline{b}_b \times \underline{b}_b \times}{\|\underline{b}_b\|^2}\right] \tag{3.3}$$

The associated magnetic moment command $\underline{m}$ sent to the coils for a desired torque $\underline{u}$ is computed as:

$$\underline{m} = \left[\frac{\underline{b}_b \times}{\|\underline{b}_b\|^2}\right] \underline{u} \tag{3.4}$$

The magnetic moment is associated to the current flow and the section of the associated coil, and is measured in Amperes-square meters (Am^2). In our notation, $(\underline{m})_i$ is the magnetic moment associated to the coil along the i-th axis. The relation between the actual torque T_{mag} and the magnetic moment $\underline{m}$ is:

$$T_{mag} = \left[-\underline{b}_b \times\right] \underline{m} \tag{3.5}$$

The matrices of the linear transformations (3.3), (3.4), and (3.5) satisfy:

Property 3.1. *For any given magnetic vector $\underline{b}_b \neq \underline{0}$ in the body frame:*

1. $\left[-\underline{b}_b \times\right] \Gamma = \left[-\underline{b}_b \times\right]$.
2. $\Gamma \left[\frac{\underline{b}_b \times}{\|\underline{b}_b\|^2}\right] = \left[\frac{\underline{b}_b \times}{\|\underline{b}_b\|^2}\right]$.
3. $\Gamma = \left[-\underline{b}_b \times\right] \left[\frac{\underline{b}_b \times}{\|\underline{b}_b\|^2}\right] = \left[\frac{\underline{b}_b \times}{\|\underline{b}_b\|^2}\right] \left[-\underline{b}_b \times\right] = \left(\left[\frac{\underline{b}_b \times}{\|\underline{b}_b\|^2}\right] \left[-\underline{b}_b \times\right]\right)^T = \Gamma^T$.
4. $\Gamma^2 = \Gamma$.

Following [23] and Property 3.1, for a given vector $\underline{b}_b$ these matrices verify:

Property 3.2. *For a given magnetic vector $\underline{b}_b \neq \underline{0}$ in the body frame:*

1. Γ *is the projection matrix onto the plane normal to* $\underline{b}_b$*, and can be written as* $\Gamma = I_3 - \frac{\underline{b}_b \underline{b}_b^T}{\underline{b}_b^T \underline{b}_b}$.
2. $\left[\frac{\underline{b}_b \times}{\|\underline{b}_b\|^2}\right]$ *is the Moore-Penrose generalized inverse [23] of the matrix* $[-\underline{b}_b \times]$*, denoted as* $[-\underline{b}_b \times]^+$.

For a given magnetic field vector $\underline{b}_b$, the relation between the desired torque $\underline{u} \in \mathcal{U} \equiv \mathbb{R}^3$, the magnetic moment $\underline{m} \in \mathcal{M}_{mag}$, and the magnetic torque $T_{mag} \in \mathcal{T}_{mag}$ can be summarized as:

$$\mathcal{U} \overset{[-\underline{b}_b \times]^+}{\longmapsto} \mathcal{M}_{mag} \overset{[-\underline{b}_b \times]}{\longmapsto} \mathcal{T}_{mag} \subsetneq \mathcal{U} \overset{\Gamma}{\longmapsto} \mathcal{T}_{mag}$$

3.3. Feedback law for three magnetorquers

Given $\epsilon, k_v > 0$ and the inertia matrix J, we select the detumbling mode torque vector $\underline{u} \in \mathbb{R}^3$ as:

$$\underline{u} \;=\; -\epsilon k_v J \underline{\omega} \tag{3.6}$$

Hence the control (3.6) determines:

$$T_{mag} \quad = \quad -\epsilon k_v \Gamma(t) J \underline{\omega} \tag{3.7}$$

Following [14], we require the orbit to be such that for any inertial pointing $\Gamma(t)$ becomes positive definite when averaged during enough time:

$$0 < \overline{\Gamma} \quad \triangleq \quad \lim_{T\to\infty} \frac{1}{T} \int_0^T \Gamma(t) dt \tag{3.8}$$

This condition can be guaranteed for near polar orbits[†] under slow enough rotations (see Lemma 1 in [14]) or using a PD control structure (see Proposition 1 in [14]). In the following we will use the averaged model by replacing $\Gamma(t)$ with $\overline{\Gamma} = \overline{\Gamma}^T > 0$.

Let us define the Lyapunov function:

$$V = \frac{1}{2} \underline{\omega}^T J^2 \underline{\omega} \tag{3.9}$$

and hence we obtain for the averaged model (replacing $\Gamma(t)$ by $\overline{\Gamma}$ in T_{mag}; see [14] for a rigorous definition)

$$\dot{V} \leq -\epsilon k_v \lambda_{min}(\overline{\Gamma}) V \tag{3.10}$$

for any $0 < \epsilon, k_v, \lambda_{min}(\overline{\Gamma})$, where $\lambda_{min}(\cdot)$ is the minimum eigenvalue. Therefore the angular velocity is exponentially stable. This result uses the general averaging theory [28] and does not require periodicity of $\Gamma(t)$, which is typically needed when using the Floquet theory on other solutions to this problem (see [29, 30, 18]).

Once the angular velocity norm $\|\underline{\omega}\|$ is smaller than a threshold $c_\omega > 0$, the Sun-pointing mode (M_2) begins. For this mode, let us consider first the fully magnetic actuation. When the CSS does not detect the Sun, i.e. during an eclipse, the control law is not modified (although a different gain can be used). On the other hand, if there is enough light detected by the CSS, we can compute the Sun vector in the body frame and use a new version of the expression (3.6) as follows[‡] (see [18]):

$$\underline{u} \quad = \quad -\epsilon^2 k_q J^{-1} \underline{q}_s - \epsilon k_v J \underline{\omega} \tag{3.11}$$

where $Q_s = [q_{0s}, \underline{q}_s^T]^T$ is the quaternion vector to point the $+Y$ solar panel toward the Sun, which is computed as follows[§]:

$$Q_s = [(\underline{s})_2, -(\underline{s})_3, 0, (\underline{s})_1]^T \tag{3.12}$$

where $\underline{s}$ is the unitary Sun vector in the body frame. In the case that $(\underline{s})_2 < 0$, Q_s is defined in the following way:

$$Q_s = [(\underline{s})_2, (\underline{s})_3, 0, -(\underline{s})_1]^T \tag{3.13}$$

[†] This is the typical case for Earth observation.

[‡] The actual gains are the products ϵk_v and $\epsilon^2 k_q$, but the reason for each factor is justified in the context of the averaging theory as applied in [14].

[§] There is abuse of notation for Q_s as we use the same symbols $Q_s = [q_{0s}, \underline{q}_s^T]^T$ for all the partial quaternion definitions.

which generates a pointing toward the $-Y$ solar panel. In the same way, it is possible to generate the vector Q_s to point toward another axis. For instance, the objective $+X$ determines[¶]:

$$Q_s = [(\underline{s})_1, 0, (\underline{s})_3, -(\underline{s})_2]^T \tag{3.14}$$

Remark 3.1. *The quaternion defined in this way is not actually the typical definition of the error between the current and desired Sun vector. In fact, the quaternion associated to the actual rotation of the Sun vector relative to* $+Y$ *in (3.12) would need to compute square roots and trigonometric functions using* $\phi_s := acos(\underline{s})_2$*:*

$$\begin{aligned} Q_s &= [q_{0s}, \underline{q}_s^T]^T = [\cos(\phi_s/2),\ -(\underline{s})_3\chi_s,\ 0,\ (\underline{s})_1\chi_s]^T, \\ \chi_s &\triangleq \begin{cases} \frac{\sin(\phi_s/2)\cdot sign((\underline{s})_2)}{\sqrt{(\underline{s})_1^2+(\underline{s})_3^2}} & when\ |(\underline{s})_2| < 1,\ or \\ 0 & otherwise \end{cases} \end{aligned} \tag{3.15}$$

Notice that here the sine/cosine of the semiangle $\phi_s/2$ *between two vectors is used, which is known as the partial quaternion in [24, 25]. We have tested the simulation with both definitions, doubling the value of the gain* k_q *when using (3.15) instead of (3.12), and the difference was numerically negligible. Due to the simplicity of the implementation, we prefer to use definition (3.12) which does not require* $\sqrt{(\cdot)}$, $\sin(\cdot)$, *and* $\cos(\cdot)$ *functions.*

3.3.1. Stability analysis

The proof of stability can be made for the averaged rigid body model, with the Lyapunov function:

$$V = 2k_q\epsilon^2(1 - |q_{s0}|) + \underline{\omega}^T J\overline{\Gamma}^{-1} J\underline{\omega} \tag{3.16}$$

where $\overline{\Gamma}^{-1}$ always exists due to the hypothesis made in (3.8), i.e., $\bar{\Gamma} > 0$. The derivative of V along the trajectories of the averaged system (replacing $\Gamma(t)$ by $\overline{\Gamma}$ in T_{mag}) is:

$$\dot{V} = -\epsilon k_v \|J\underline{\omega}\|^2 - \underline{\omega}^T J\overline{\Gamma}^{-1}(\underline{\omega} \times J\underline{\omega}) \pm k_q\epsilon^2(\underline{\omega}_s - \underline{\omega})^T \underline{q}_s \tag{3.17}$$

In the third term the vector $\underline{\omega}_s$ gives the angular velocity for the quaternion $\underline{q}_s$, and therefore the expression in parenthesis $(\underline{\omega}_s - \underline{\omega})$ is orthogonal to $\underline{q}_s$ by definition. The sum of the first two terms is negative provided:

$$0 < \|\underline{\omega}\| < C_\omega \triangleq \frac{\epsilon k_v \underline{\sigma}(\overline{\Gamma})}{\sin(\beta_J^*)} \tag{3.18}$$

where β_J^* is the maximum angle between $\underline{\omega}$ and $J\underline{\omega}$ [26]:

$$\beta_J^* = \text{acos}\left(\frac{2\sqrt{\kappa_J}}{1+\kappa_J}\right) \tag{3.19}$$

where κ_J is the condition number of J, which is always well-defined as $J > 0$. The bound (3.18) can be found to be around five times the orbital angular velocity (see [18]), which gives a criteria

---

[¶] It can be defined for any axis, not necessarily canonic.

for the selection of the threshold $c_\omega \ll C_\omega$ to commute between the detumbling mode M_1 to the Sun-pointing mode M_2. As the Lyapunov function does not depend on time explicitly, this also guarantees the asymptotic stability using the Barbashin-Krasovskii-LaSalle theorem extended for a class of non-autonomous systems in [27].

The stability can also be shown in terms of the alternative quaternion pair (3.12)–(3.13) with:

$$V \;=\; 2k_q\epsilon^2(1 - |(\underline{s})_2|) + \underline{\omega}^T J\overline{\Gamma}^{-1} J\underline{\omega} \tag{3.20}$$

where $\dot{\underline{s}} = -\underline{\omega} \times \underline{s}$ and hence for the case (3.12) with objective $(\underline{s})_2 = +1$ we obtain:

$$-2k_q\epsilon^2(\dot{\underline{s}})_2 = -2k_q\epsilon^2 \left((\underline{\omega})_1(\underline{s})_3 - (\underline{\omega})_3(\underline{s})_1\right) \tag{3.21}$$

which cancels with the term in $\dot{V}$ associated with the proportional control:

$$2\underline{\omega}^T J\overline{\Gamma}^{-1}\overline{\Gamma}J^{-1}\left(-k_q\epsilon^2[-(\underline{s})_3,\ 0,\ (\underline{s})_1]^T\right) \tag{3.22}$$

in the derivative of the Lyapunov function. The same stability can be obtained with the other branch of the absolute value in the first term of V, using the objective $(\underline{s})_2 = -1$ and the associated quaternion (3.13). The capability to switch between the two opposite solar panels makes the convergence faster to the desired power generation levels. In order to keep the stability under switching, we define a minimum dwell time to maintain the same pointing objective, in order to obtain a slow enough switch (see [31]). Once a change is made, it is not allowed during the following orbit period.

The magnetic moment allocation is made preserving the vector direction. This means that if the j-th component of $\underline{m}$ were higher than the maximum moment given by the j-th coil m_j^+, the following vector saturation applies:

$$(\underline{m})_i := (\underline{m})_i|(\underline{m})_j|^{-1}m_i^+,\ \forall i = 1, 2, 3 \tag{3.23}$$

which is in turn evaluated over the remaining $j \in \{1, 2, 3\}$. We will not consider here the stability analysis under saturation and a bounded actuator, but it can be seen from simulation results that only the detumbling mode might reach these limits. For this analysis, it is straightforward to see that (3.10) will be attenuated by a factor (lower or equal to 1) proportional to the combined attenuation made over all the axes after saturation, which preserves the exponential stability over a bounded set of initial conditions (i.e., the initial angular velocity norm has a known bound).

3.4. Feedback law for three magnetorquers and one wheel

As mentioned in the introduction, in the textbook [13] (Section 7.4) it is claimed that the combination of three magnetorquers with one wheel provides full controllability at every time on a low Earth orbit. However, this is not actually true, since when $\underline{k}_w^T\underline{b}_b = 0$, there are only two control torque directions available. This can be extended to the case with a second wheel with axis $\underline{k}_{w*}$ such that $\underline{k}_w^T\underline{b}_b = \underline{k}_{w*}^T\underline{b}_b = 0$, although we will restrict ourselves to the single wheel case.

Let *iw* be the axis index where the single reaction wheel is installed. The reaction wheel control is given by:

$$T_w \;=\; -\epsilon^2 k_q(J^{-1}\underline{q}_s)_{iw} - \epsilon k_v(J\underline{\omega})_{iw} + T_d(H_w) \tag{3.24}$$

When there is an eclipse, the control is limited to the derivative term only, as before. In this law, the term $T_d(H_w)$ compensates the wheel's drag torque with a model function of the wheel momentum H_w. This can also be written in terms of the wheel speed, but it was defined in this way to relate with the simulator variables, without loss of generality.

The need to unload the kinetic moment of the wheel is well known, otherwise it would saturate and lead to the loss of controllability on that axis. The momentum management law is implemented assuming the measurement of the wheel's speed and knowing its inertia $J_w \in \mathbb{R}_{>0}$ to estimate its kinetic moment as $\hat{H}_w = J_w \Omega_w$, where Ω_w is assumed to be available in real time. An unloading term u_w^{un} is added to the right-hand side of (3.11) on the axis *iw* (i.e., the wheel's axis):

$$u_w^{un} = -K_w^{un} \hat{H}_w \tag{3.25}$$

where $K_w^{un} > 0$ is the unloading gain. On the other hand, the magnetic torque generated by this unloading law is subtracted from the commanded torque to the wheel, in order to unload its momentum and cancel any net torque on the spacecraft. The selection of the gain K_w^{un} may be done as the following [33]:

$$K_w^{un} = \frac{k}{||\underline{b}_b||^2 \sin^2(\alpha)} \tag{3.26}$$

where k is the desired bandwidth of the speed function to be attenuated and α is the angle between the wheel's axis and the vector $\underline{b}_b$. For the selected orbit, we may assume $\sin^2(\alpha) < 0.75$, $||\underline{b}_b|| < 0.000045$ T, and $k = 0.00008$ rad/sec, and hence we select the minimum gain from these bound:

$$K_w^{un} = \frac{0.00008}{0.000045^2 \cdot 0.75} \approx 5 \cdot 10^4 \tag{3.27}$$

The bandwidth k means a period around 13 times larger than the orbit period, and hence the unloading should be effective for speed evolutions slower than this bound. Notice that this k is therefore one order of magnitude higher than the expected attitude control convergence rate for a Sun-pointing objective. Also, the parameter k may be related to the ratio between the maximum torque disturbance and the maximum wheel kinetic moment to be unloaded in these conditions (see [33]). Due to the need to unload the effect of a greater disturbance, we select $K_w^{un} = 2.5 \cdot 10^5$ when the wheel is mounted along the $\pm X$ or $\pm Y$ axes.

As the quaternion defined to point any of the panels to the Sun does not measure the angle around this axis, it is possible to induce an angular velocity around $\pm Y$ on this spacecraft. However, in order to keep the validity of the magnetic control (angular velocities must be smaller than the orbit angular velocity, see [14]), we select angular velocities lower than half of the orbit angular velocity, which for polar orbits means around one quarter of the magnetic field turn rate (as there are two turns of the magnetic field vector per orbit). This defines the mode M_3, which has on both conditions (eclipse or not) the following additional term:

$$\underline{u}_{M_3} = \underline{u}_{M_2} + \epsilon k_v J \underline{\omega}_r \tag{3.28}$$

where for instance $\underline{\omega}_r = [0\ \rho\ 0]^T \omega_o$, with ω_o being the orbital angular velocity. Notice that for $|\rho| = 1$ and a dawn/dusk orbit, this mode may provide a coarse pointing of the $+Z$ axis toward the zenith.

3.4.1. Stability analysis

Notice that the dynamics of the spacecraft with one wheel (3.2) has the following additional term:

$$-\underline{\omega} \times H_w \underline{k}_w \tag{3.29}$$

which may be compensated for by the magnetic control adding a term in (3.11) as follows:

$$\underline{u} = -\epsilon^2 k_q J^{-1} \underline{q}_s - \epsilon k_v J \underline{\omega} + \overline{\Gamma}^{-1} (\underline{\omega} \times H_w \underline{k}_w) \tag{3.30}$$

In this way, the same stability analysis holds considering that the extra terms due to the wheel plus the magnetic control can be written replacing $\Gamma(t)$ by $\overline{\Gamma}$ (its average) as:

$$\overline{\Gamma}\underline{u} + (T_w - T_d(H_w))\underline{k}_w - \underline{\omega} \times H_w \underline{k}_w = (\overline{\Gamma} + g_w \underline{k}_w \underline{k}_w^T)(-k_q \epsilon^2 J^{-1} \underline{q}_s - \epsilon k_v J \underline{\omega}) \tag{3.31}$$

where $g_w > 0$ can be specified to improve the response of the axis with the reaction wheel. In this way the same stability proof is valid with the following Lyapunov function:

$$V = 2k_q \epsilon^2 (1 - |q_{s0}|) + \underline{\omega}^T J (\overline{\Gamma} + g_w \underline{k}_w \underline{k}_w^T)^{-1} J \underline{\omega} \tag{3.32}$$

whose derivative is (3.17) and the same stability arguments can be applied. From a practical point of view, we have seen by simulations that the effect of the compensation of the term (3.29) is negligible in $\dot{V}$. From an analytic point of view, this can be guaranteed if:

$$\left| \underline{\omega}^T J (\overline{\Gamma} + g_w \underline{k}_w \underline{k}_w^T)^{-1} (\underline{\omega} \times H_w \underline{k}_w) \right| \ll k_v \| J \underline{\omega} \|^2 \tag{3.33}$$

The mode M_3 is only considered using the reaction wheel and magnetorquers as actuators. The associated stability proof can be made with the following Lyapunov function defined with $\delta\underline{\omega} = \underline{\omega} - \underline{\omega}_r$:

$$V = 2k_q (1 - |q_{0s}|) + \delta\underline{\omega}^T J \left(\overline{\Gamma} + g_w \underline{k}_w \underline{k}_w^T \right)^{-1} J \delta\underline{\omega} \tag{3.34}$$

As $\delta\underline{\dot{\omega}} = \underline{\dot{\omega}} - \underline{0} = \underline{\dot{\omega}}$, we obtain:

$$\dot{V} = -k_v \| J \delta\underline{\omega} \|^2 + \delta\underline{\omega}^T J (-\underline{\omega} \times (J \underline{\omega} + H_w \underline{k}_w)) \pm k_q \epsilon^2 (\delta\underline{\omega}_s - \delta\underline{\omega})^T \underline{q}_s \tag{3.35}$$

Notice that the third term is zero as before, while the second term can be compensated with the control:

$$\underline{u} = -\epsilon^2 k_q J^{-1} \underline{q}_s - \epsilon k_v J \delta\underline{\omega} + (\overline{\Gamma} + g_w \underline{k}_w \underline{k}_w^T)^{-1} \left(\underline{\omega} \times (J \underline{\omega} + H_w \underline{k}_w) \right) \tag{3.36}$$

In the numerical simulations we found negligible the effect of the compensation in the last term of (3.36). From an analytic point of view, a sufficient condition to justify this observation is:

$$\left| \delta\underline{\omega}^T J \left(\overline{\Gamma} + g_w \underline{k}_w \underline{k}_w^T \right)^{-1} \left(\underline{\omega} \times (J \underline{\omega} + H_w \underline{k}_w) \right) \right| \ll k_v \| J \delta\underline{\omega} \|^2 \tag{3.37}$$

3.4.2. Speed vs. torque command

A reaction wheel may accept torque commands, which are translated directly into current on the wheel motor, or speed commands which determine the target speed to be achieved by an internal loop which uses the motor current as the input and the wheel's speed as the output. Notice that in the first case the motor current, and therefore the motor torque, does not translate directly into a torque in the spacecraft, as the heat produced by friction produces a drag torque which is opposite to the motor torque and reduces the net torque on the spacecraft. On the other hand, not any speed can be commanded in closed-loop operation, as the wheel's motor's maximum torque determines a maximum feasible wheel speed modulus. The 42 simulator only considers the torque command, but we will see that it is possible to translate the torque command into a speed command.

Speed Command: Modern reaction wheels compensate for the drag term internally in a closed loop with accurate models. In particular, if the wheel has closed-loop speed control, see [35], the torque T_w is transformed into a speed command knowing the previous speed and the wheel rotor inertia as:

$$\Omega(t_k) = \Omega(t_{k-1}) - J_w^{-1} T_w(t_k)(t_k - t_{k-1}) \tag{3.38}$$

where $\{t_k, k \in \mathbb{N}\}$ is the sequence of control times. In (3.38) we have assumed that the wheel axis orientation is along the $+Z$ axis, so the increase of wheel speed reduces the spacecraft angular velocity around $+Z$. The actual command sent to the wheel must be saturated as a function of the speed difference (i.e., the available torque) as:

$$|T_w(t_k)| \leq T_w^+ - |T_d(J_w\Omega(t_k))| \text{ when } T_w(t_k)\Omega(t_k) \leq 0, \tag{3.39}$$

$$|T_w(t_k)| \leq T_w^+ + |T_d(J_w\Omega(t_k))| \text{ when } T_w(t_k)\Omega(t_k) > 0. \tag{3.40}$$

Here we would need to have some knowledge on the drag term. In order to simplify the implementation, we have adopted a maximum torque of $\frac{1}{10}T_w^+$ always in order to avoid the need of a drag model and considering that the selected wheel torque is oversized in comparison with the satellite inertia around the Z axis. This simple strategy was enough for the control modes of USAT-I, verified by simulations.

Torque Command: In order to complete the analysis, we considered also the possibility of a wheel with an open-loop torque command, which has to compensate externally for the drag term with an adaptive control law. To this end, we propose the following model for the wheel's drag torque effect compensation:

$$T_d(H_w) = -\hat{a}_w H_w |H_w| \tag{3.41}$$

where $\hat{a}_w$ is an estimation of the dynamic friction parameter. When the wheel reaches its maximum torque capacity, it is not feasible to increase its speed. The maximum velocity is realized when the torque absolute value of the wheel equals its associated drag torque, and hence the following relation holds:

$$|T_w^+| = T_d(H_w^+) = \hat{a}_w (H_w^+)^2 \tag{3.42}$$

where T_w^+ is the maximum torque and H_w^+ the maximum moment of the wheel. Hence:

$$\hat{a}_w = T_w^+ (H_w^+)^{-2} \tag{3.43}$$

In the case where this estimation is uncertain, it could be taken as the initial value for an adaptive law. Let V_a be the modified Lyapunov function to estimate a_w with $\hat{a}_w$:

$$V_* = V + \frac{\tilde{a}_w^2}{2p_w} \tag{3.44}$$

where $\tilde{a}_w = \hat{a}_w - a_w$ and $p_w > 0$ is a constant to be determined. We consider the true value $a_w \in \mathbb{R}_{>0}$ constant, so $\dot{\tilde{a}}_w = \dot{\hat{a}}_w$ and:

$$\dot{V}_* = \dot{V} + \underline{\omega}^T J \overline{\Gamma}^{-1} \underline{k}_w \left(-\tilde{a}_w H_w |H_w|\right) + \frac{\tilde{a}_w}{p_w} \dot{\hat{a}}_w \tag{3.45}$$

Following [34], we define the estimator to cancel the last two terms:

$$\dot{\hat{a}}_w = p_w H_w |H_w| \underline{\omega}^T J \overline{\Gamma}^{-1} \underline{k}_w \tag{3.46}$$

In order to make the adaptation more robust, it may be constrained between ±15% of $\hat{a}_w(t_0)$, which was evaluated by simulation. As mentioned before, this was not necessary for the wheel adopted for USAT-I and is provided only as a simulation case.

4. Implementation in 42

The 42 simulator is a free simulator of spacecraft attitude, orbit dynamics, and environmental models developed by Erik Stoneking at NASA's Goddard Space Flight Center [16]. It supports spacecraft models composed of multiple flexible bodies, slosh, multiple spacecraft, inter-spacecraft links, different flight regimes (two-body, planetary surfaces, asteroids, etc.), and provides visualization among many other capabilities not required for our simple simulation scenario.

Moreover, it can separate the flight software from the simulator of the spacecraft and the display in different applications or even different computers. This makes this simulator relatively straightforward to begin mission analysis but also powerful enough to support the development of the flight software and the ACS subsystem, and also to help the flight engineering operations group. This simulator is also part of the OpenSatKit framework specific for the CubeSats, as detailed in [17].

In our case, this simulator was selected due to its capability to cover the initial mission analysis for the ACS discipline and also to develop and test the flight software in C language. The set of actuators and sensors was enough to cover all the features of this CubeSat mission, while the simulation examples were provided with controller functions which were very helpful to understand implementation details. Finally, the simulator is useful to make easier the exchange of information of the subsystem, as the input files contain a good description of the control loop elements. This allowed us to make trade-off studies as is typically made on the three first formulation phases of a space project (i.e., pre-phase A, phase A, and phase B). The definitions of the control functions included in the simulation are provided as complementary material to this paper.

The following table shows the saturation values for the spacecraft actuators:

Table 2. USAT-I actuator saturation values.

MTB-X magnetic moment	0.24 Am^2
MTB-Y magnetic moment	0.24 Am^2
MTB-Z magnetic moment	0.13 Am^2
RW-Z torque	0.00023 Nm
RW-Z angular momentum	0.00177 Nms

These and other parameters are specified on the simulation input files, as described in the Appendix.

5. Simulation results

In this section we show the main results using the numerical simulator. Figure 4 shows the mean power factor as a function of the RAAN for a given date, which can be interpreted as the local hour between 6am/pm and 12am/pm. The dashed lines show the minimum over one orbit, and the continuous line the stationary averaged over 22 orbits. The red lines correspond to the magnetic control, and the blue line to the magnetic control plus one reaction wheel. This highlights the robustness of the solution using one wheel compared to the magnetic-only control.

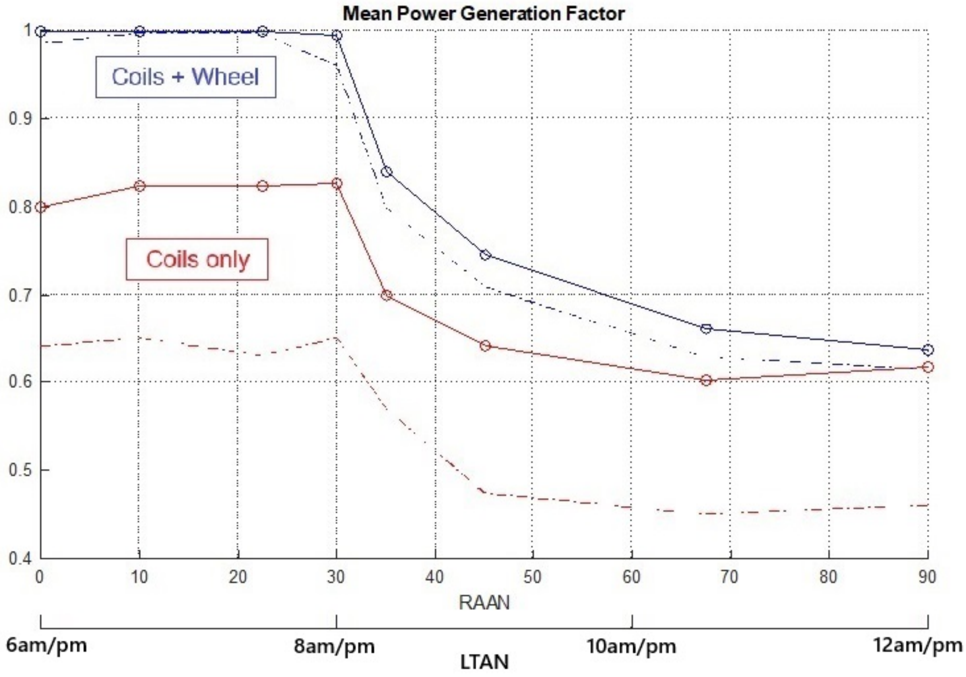

Figure 4. Power generation factor vs. RAAN (or LTAN) on a range of SSO orbits. Continuous lines show orbit averages, while dashed lines represent the minimum values.

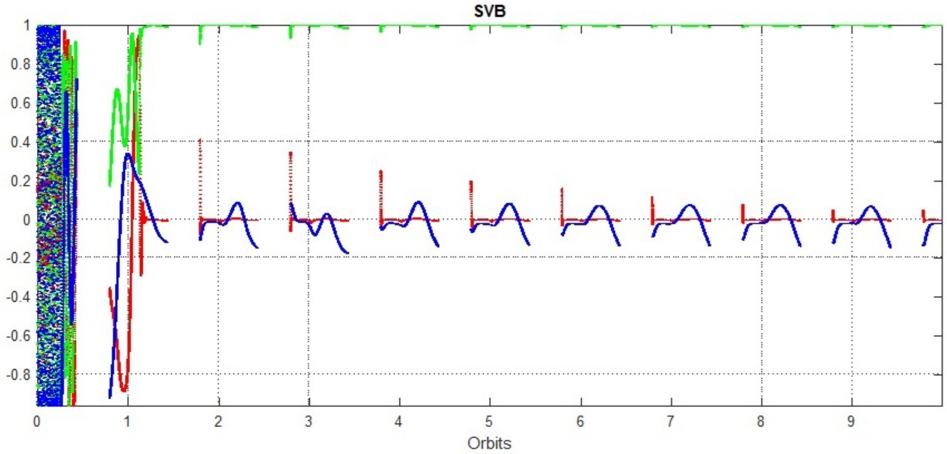

Figure 5. Sun vector components in the body frame for a 600km SSO orbit with maximum eclipse (i.e., a local hour at noon). The Y axis is in green (Sun objective $\pm Y$), X in red, and Z in blue.

In particular, the Sun vector components in Figure 5 when using the wheel may be directly compared with the same components in Figure 7 when the wheel is not used. The solar panels allow us to generate power for $+Y$ and $-Y$ (Y axis in green, X in red, and Z in blue).

Figure 6 shows the magnetic moment, wheel speed, and the spacecraft angular velocity for the control case using magnetorquers and one wheel during the first two orbits on which there is an eclipse.

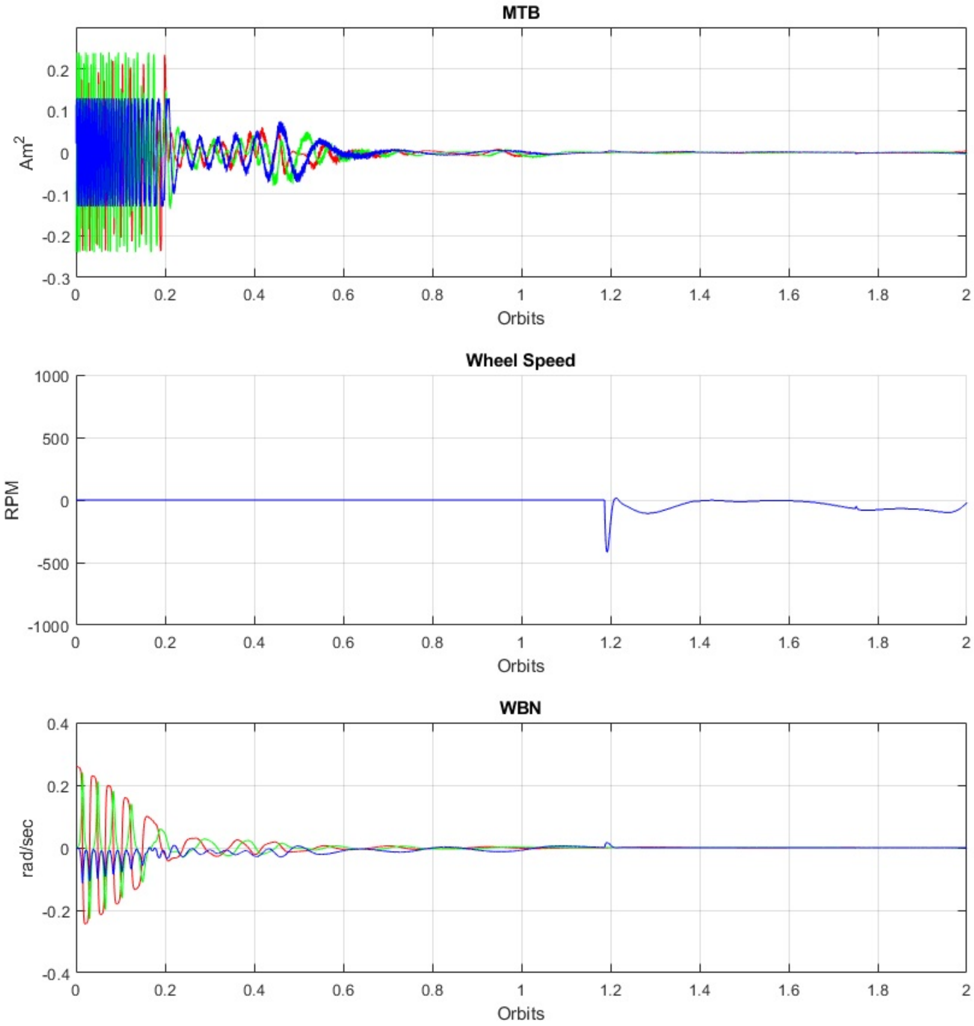

Figure 6. Magnetic coils momentum (up), reaction wheel (middle), and angular velocity components (bottom), using red (X), green (Y), and blue (Z) colors.

Notice that for the latter case the power generation may still guarantee a minimum mean value, but the behavior of the Sun vector components may be chaotic. The green component (Y) may have sign transitions on the eclipses (not shown) or even over the three-axis controlled phase. Due to this fact, the objective is selected toward $+Y$ or $-Y$ in order to minimize the angular transition. The wheel can be installed on any axis—these simulations were made with the wheel in the $+Z$ axis using $K_w^{un} = 10^5$ but the results are similar to those with the wheel in the $+Y$ axis, changing the moment unloading gain to $K_w^{un} = 5 \cdot 10^5$. In the case of mode M_2 using an orbit without eclipse, it was better to use the wheel on the Z axis. The other gains were selected as follows:

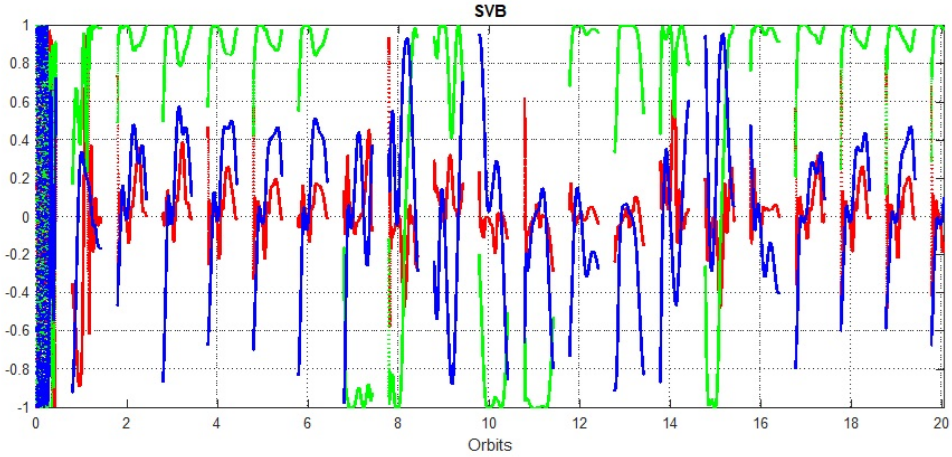

Figure 7. Resulting Sun vector when the wheel is not used, using red (X), green (Y), and blue (Z) colors.

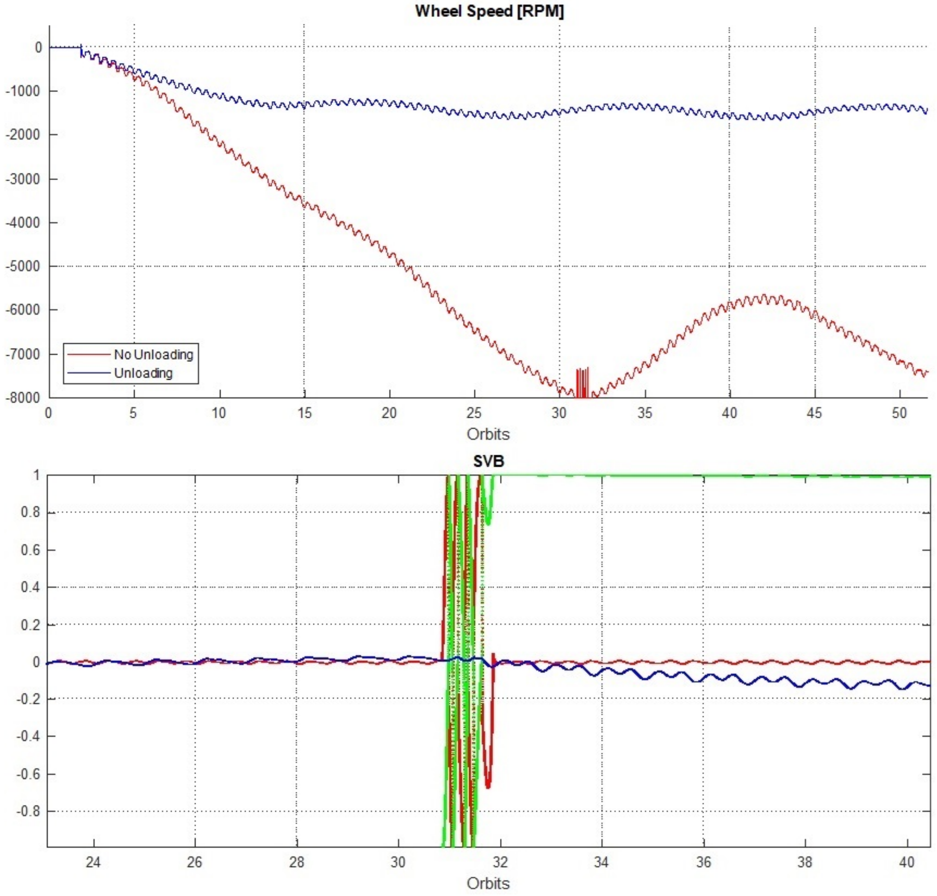

Figure 8. The upper figure shows the resulting wheel speed with and without momentum unloading. The lower figure shows the Sun vector in the body frame (X: red, Y: green, Z: blue).

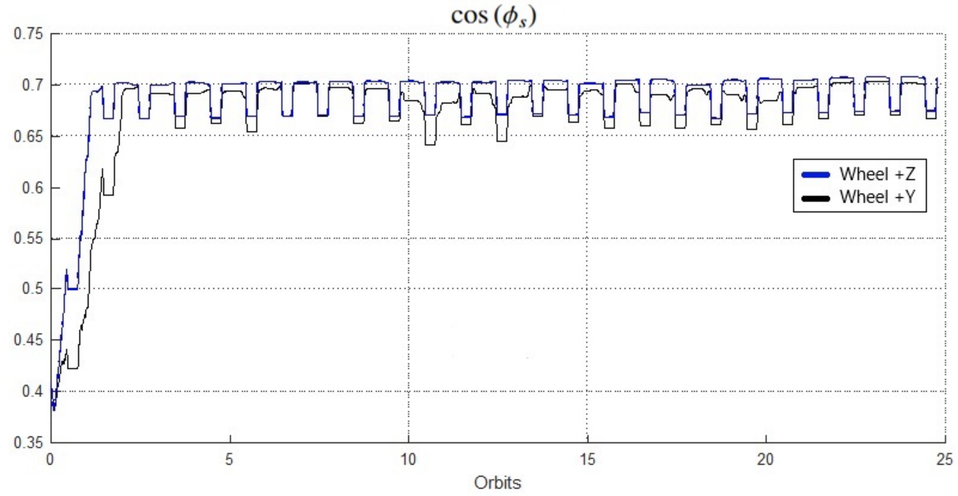

Figure 9. Power factor for a local hour around 14:30 hs, with two options of reaction wheel locations.

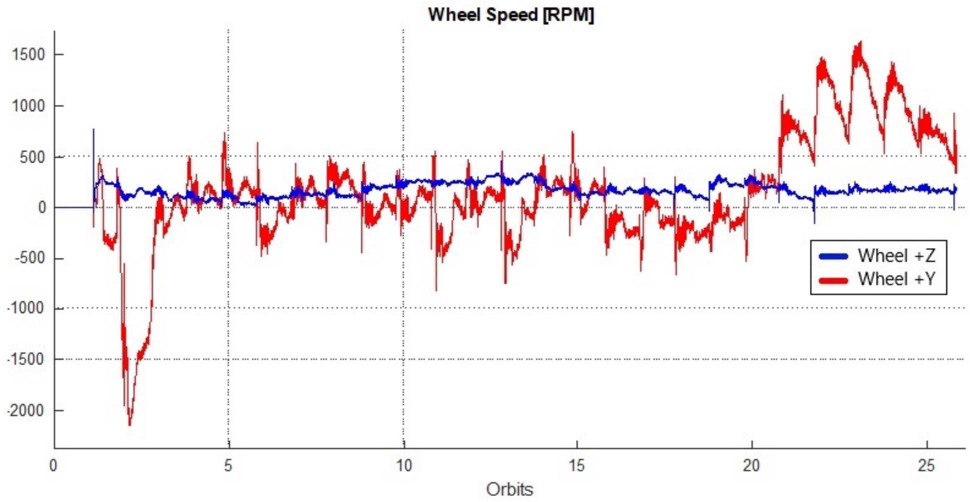

Figure 10. Wheel speed for a local hour around 14:30 hs, with two options of reaction wheel locations.

- Mode M_1: $k_w = 10$, $\epsilon = 0.001$, and $c_\omega = 0.001$ rad/sec. A smaller value for $c_{\overline{\omega}}$ may determine a delayed transition, while we consider this threshold slow enough to obtain a good initial condition for the Sun-pointing mode M_2.
- Mode M_2: the following gains were used: $\epsilon = 0.001$, $k_w = 5$, and $k_q = 0.0075$. The threshold to detect the Sun using the sum of illumination from all the CSSs was set at half of the maximum possible value of one cell.
- Mode M_3: the gains were set as in Mode 2, setting $\rho = 1.0$ after three and a half orbits. In this way, it is possible to point $+Z$ near to the nadir (keeping the Sun-pointing, hence this nadir pointing error can be minimized near the equinox dates, with maximum errors near the solstices).
- Wheel axis: the k_w, k_q gains on the wheel axis are scaled by 5.

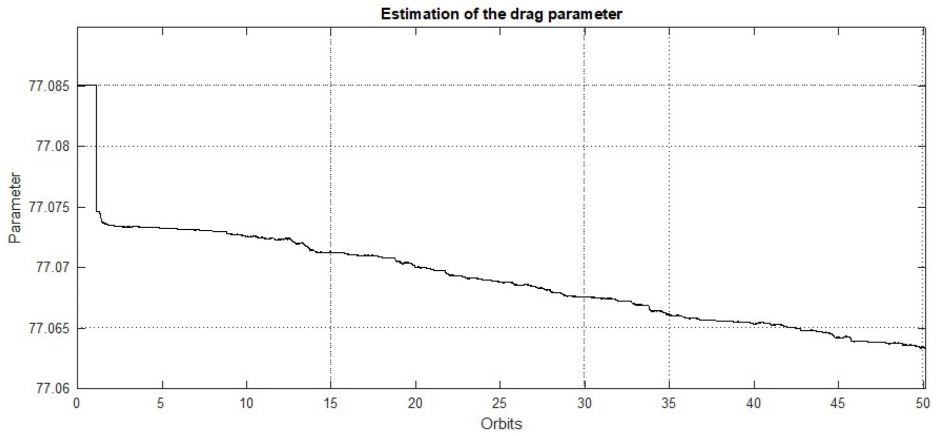

Figure 11. Wheel drag parameter estimation, being the true value 73.41.

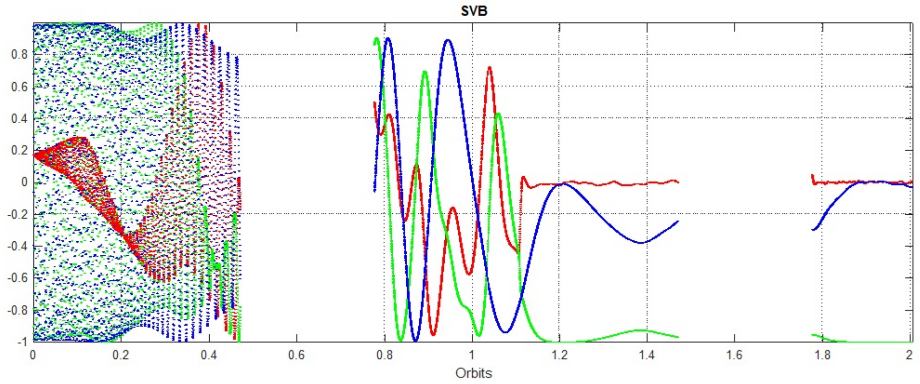

Figure 12. Sun vector components during the first two orbits, using red (X), green (Y), and blue (Z) colors.

The results show that for RAAN = 55° (a local hour around 14:30 hs for this simulation) the power factor and the wheel speed shown in Figure 9 and Figure 10, respectively, are better when using the wheel on the $+Z$ axis instead of the $+Y$ axis. The difference may be explained due to the need of a gain adjustment in the case of the $+Y$ axis, which is not necessary for the wheel on the $+Z$ axis. Also, the fact that the smaller inertia determines a greater sensitivity to disturbances and/or lack of controllability validates the simulation results, as the wheel on the $+Z$ axis makes it possible to compensate quickly for any disturbance on this highly sensitive axis. The maximum wheel torque is $T^+_{rw} = 0.00023$ Nm and the maximum wheel momentum is $H^+_{rw} = 0.00177$ Nms. The moment unloading benefits are clearly shown in Figure 8. The lower figure shows the effect of the speed saturation on the Sun vector, using red (X), green (Y), and blue (Z) colors. This shows also the effect of not using momentum management for the wheel, which induces eventually a loss in controllability due to the momentum saturation.

The 42 simulator considers a torque command for the wheels. The drag model was simulated with $a_w = T^+_w(H^+_w)^{-2} = 73.4$; the results were robust even when the drag was not exactly compensated due to the unknown a_w by ±5%. Also we tested the estimator configured with $p_w = 10^8 \cdot J^2_w\overline{\Gamma}_{2,2}$. The evolution of the estimation is shown in Figure 11, using $a_w(t_0) = 77.0851$. Notice that the estimation does not converge to the true value, which is typical on this type of adaptive control where the adaptation is made only when there is enough information and aiming to obtain stability of the control error, but not for the estimation error (see Chapter 8 in [34]).

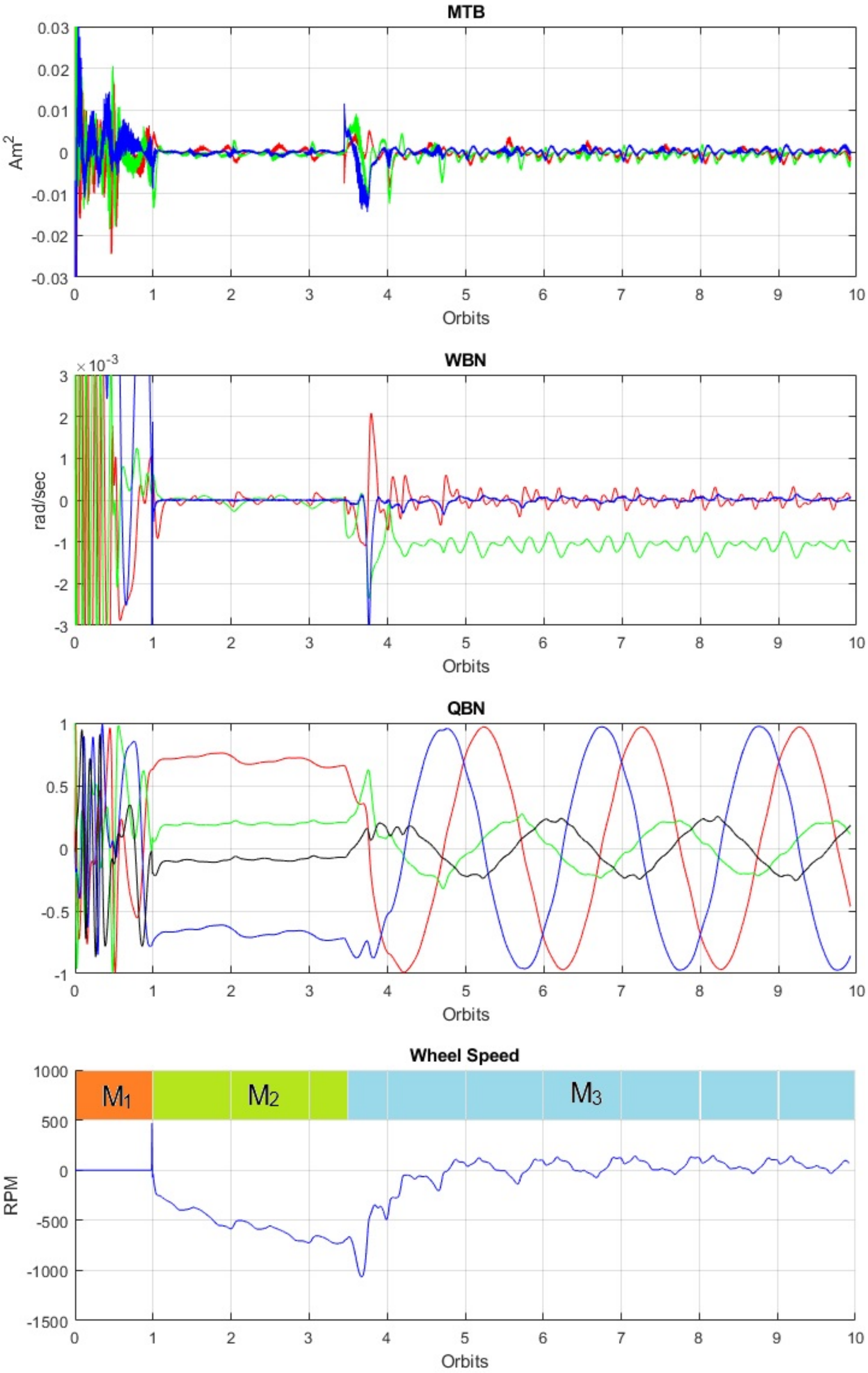

Figure 13. Mode M_1 (detumbling) on the first orbit, followed by Mode M_2 (Sun-pointing on the $+Y$ axis), and finally Mode M_3, commanded after three and a half orbits.

The Sun vector for the first two orbits is shown in Figure 12, for an SSO orbit with an eclipse duration around 30 min, with an initial angular velocity vector $\underline{\omega}(t_0) = [20°/s, 0, 0]^T$.

Figure 13 shows a simulation for a dawn/dusk orbit on which it is possible to configure the angular velocity around the vector pointing to the Sun, which allows us to obtain a coarse point to a certain zone in the Earth while keeping the pointing of the solar panels to the Sun. The $+Y$ axis is pointed to the Sun with one orbital angular velocity ($\rho = 1$) around $+Y$. For all the axes we have used red for X, green for Y, and blue for Z, while the scalar component of the quaternion is in black. The range of the magnetic moment and angular velocity are zoomed in to show more detail.

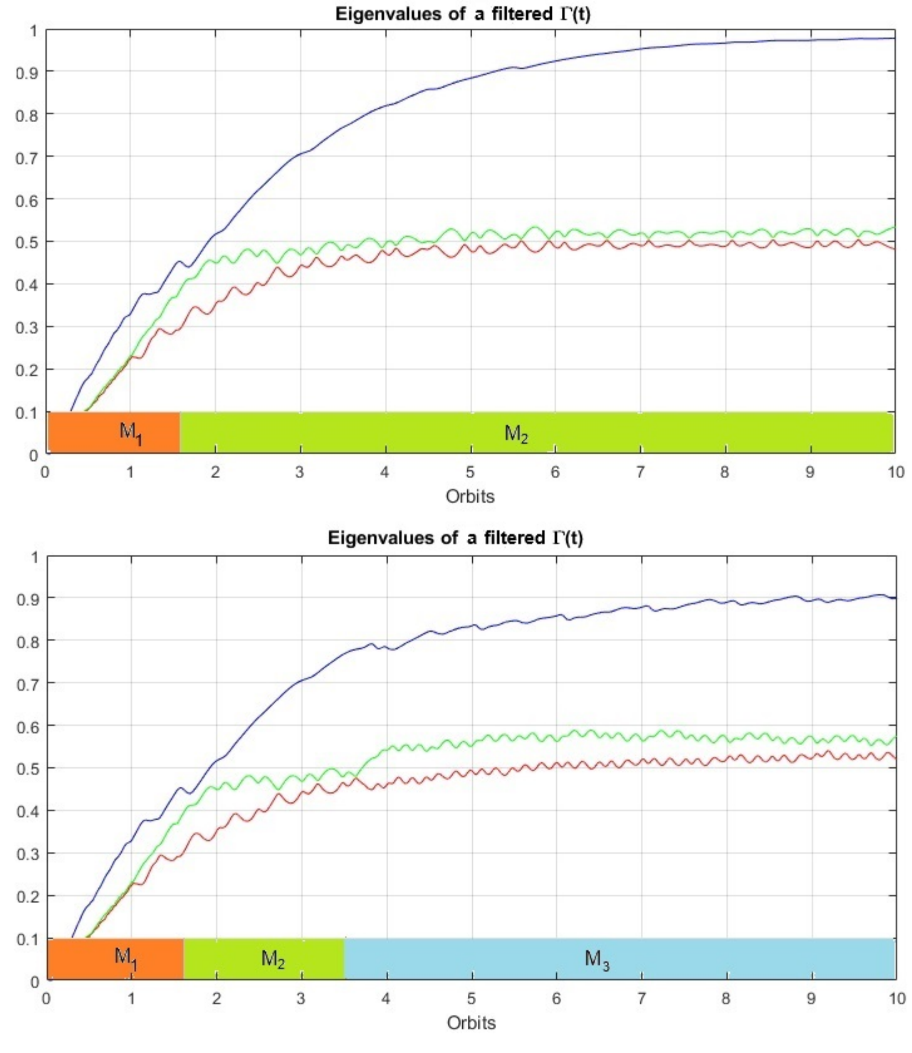

Figure 14. Comparison of eigenvalues of a low-pass filtered matrix $\Gamma(t)$ for a transition $M_1 \rightarrow M_2$ (up) and a transition $M_1 \rightarrow M_2 \rightarrow M_3$, showing almost the same behavior.

Moreover, it is feasible to obtain a coarse pointing to the zenith in order to improve the acquisition of GNSS satellites, which can also be simulated numerically (see [36]). This real-time orbital information is not exploited in this mission, but can be used post-facto to test technology for autonomous orbit control [37, 38]. The transition between M_1 and M_2 happens after one orbit period and is defined when the norm of the angular velocity falls below one orbital angular velocity, which is considered small enough to transition to an inertial pointing. The transition between M_2 and M_3 happens after 3.5 orbital periods.

Finally, notice that the stationary angular velocity of M_3 is not negligible (in fact it is the orbital velocity), and hence it might not be guaranteed that $\overline{\Gamma} > 0$ (see [14]). Figure 14 shows the eigenvalues of a low-pass filtered $\Gamma(t)$, showing almost the same behavior for the (inertial) Sun-pointing (upper plot) compared with the transition to the M_3 (non-inertial) Sun-pointing with rotation at the orbital rate. The colors are ordered from lower to higher values, being blue for the Y eigenaxis, while red and green are for eigenaxes on the (X, Z) plane. The greater value (in blue) is associated to an eigenaxis with a main component on the Y axis. The lower value (red) is associated to the eigenaxis on Z, with smaller components on the X and Y axes. The remaining value (green) has an eigenvector mainly on X with smaller components on the Z and Y axes. However, these two lower values are too close so they can be associated approximately to the (X, Z) plane. This result gives insight on the reason of the selection of the wheel on the Z axis, as it provides torque on the subspace with lowest magnetic control authority. The evaluation of the matrix $\overline{\Gamma} + g_w \underline{k}_w \underline{k}_w^T$, not shown, increases the eigenvalue associated to the Z axis by g_w.

6. Conclusions

This work analyzed the possible configuration of actuators and control laws on the 3U USAT-I CubeSat. Three control modes were considered, including detumbling (M_1), Sun-pointing (M_2), and Sun-pointing with an orbital angular velocity (M_3, to attain a coarse nadir pointing of $+Z$ axis). As for this low-cost project the final orbit cannot be guaranteed, the feasibility of the M_3 mode and the S-band downlink depend on achieving a dawn/dusk SSO orbit, but the control law was adapted to attain it in this scenario, while the operation of the spacecraft was assumed feasible with the UHF link only.

The fully magnetic control was compared with the addition of one reaction wheel, leading to a significant improvement when the reaction wheel was mounted along the longer axis (lowest inertia) of the satellite, regardless of the local hour of the orbit (i.e., the duration of the eclipse). As a second option, when the reaction wheel was mounted along the axis pointing to the Sun (one of the axes with higher inertia); the same advantage was obtained for the orbit with largest eclipse durations, but the behavior degraded as long as the orbit reduced the eclipse duration. The justification we see for this behaviour is that the underactuation determined by the magnetic control becomes less robust on the spacecraft axis with the smallest inertia.

Although these attitude control feedback laws are well-known in the literature, we showed their stability to help the understanding of the alternatives, based on previous results, and presented an implementation using NASA's 42 simulator. The source files with the control function and the simulator input files are also provided as auxiliary files to be downloaded.

This tool allows us to cover all the development to test quickly several possible feedback laws and hardware configurations, obtaining as a result a control routine in C language compatible with the implementation on the flight processor and its validation through software and hardware in the loop.

Author contributions

Both authors contributed to the study conception, analysis, simulation, and validation.

Use of AI tools declaration

The authors declare they have not used Artificial Intelligence (AI) tools in the creation of this article.

Acknowledgments

This work was supported by the Universidad Nacional de La Plata (UNLP), Comisión Nacional de Actividades Espaciales (CONAE), and Secretaría de Innovación, Ciencia y Tecnología de Argentina.

Conflict of interest

The authors declare no conflict of interest.

References

1. Alvarez D, Aguilar-Nadalini A, Bagur J, et al. (2023) Design and On-Orbit Performance of the Attitude Determination and Passive Control System for the Quetzal-1 CubeSat. *J Small Satell* 12: 1231–1247. https://jossonline.com
2. Carletta S, Nascetti A, Gosikere Matadha SS, et al. (2022) Characterization and Testing of the Passive Magnetic Attitude Control System for the 3U AstroBio CubeSat. *Aerospace* 9: 723. https://doi.org/10.3390/aerospace9110723
3. Alarazah H (2018) Theoretical and Numerical Analysis of the Attitude Control of a 3U CubeSat - Iraqi Satellite (TIGRISAT). *Association Arab Universities J Eng Sci* 25.
4. Riano-Rios C, Sun R, Bevilacqua R, et al. (2021) Aerodynamic and gravity gradient based attitude control for CubeSats in the presence of environmental and spacecraft uncertainties. *Acta Astronautica* 180: 439–450. https://doi.org/10.1016/j.actaastro.2020.12.038
5. Sutherland R, Kolmanovsky I, Girard AR (2019) Attitude Control of a 2U Cubesat by Magnetic and Air Drag Torques. in *Ieee T Contr Syst Technol* 27: 1047–1059. https://doi.org/10.1109/TCST.2018.2791979
6. Gaude A, Vaios L (2020) Design and Structural Analysis of a Control Moment Gyroscope (CMG) Actuator for CubeSats. *Aerospace* 7: 55. https://doi.org/10.3390/aerospace7050055
7. Grau S, Kapitola S, Weiss S, et al. (2021) Control of an over-actuated spacecraft using a combination of a fluid actuator and reaction wheels. *Acta Astronaut* 178: 870–880. https://doi.org/10.1016/j.actaastro.2020.10.018
8. Gatsonis N, Lu Y, Blandino J, et al. (2014) Cubesat Design and Attitude Control with Micro Pulsed Plasma Thrusters. In: *AIAA SPACE 2014 Conference and Exposition.* https://doi.org/10.2514/6.2014-4211
9. Avanzini G, de Angelis E, Giulietti F, et al. (2019) Attitude control of Low Earth Orbit satellites by reaction wheels and magnetic torquers. *Acta Astronaut* 160: 625–634. https://doi.org/10.1016/j.actaastro.2019.03.013
10. El-wafi I, Haloua M, Guennoun Z, et al. (2024) A framework for developing an attitude determination and control system simulator for CubesSats: Processor-in-loop testing approach. *Results Eng* 22: 102201. https://doi.org/10.1016/j.rineng.2024.102201

11. Botta S, Actis M, Rogers W, et al. (2021) USAT I - Avances en el primer satélite de la UNLP, 6^{to} *Congreso Argentino en Ingeniería Aeronáutica*, UTN Haedo.

12. Hu Y, Jiang Z, Yuan X (2024) Isometric mapping algorithm based GNSS-R sea ice detection. *Metasci Aerosp* 1: 38–52. https://doi.org/10.3934/mina.2024002

13. Sidi M (1997)*Spacecraft Dynamics and Control: A Practical Engineering Approach*, Cambridge University Press.

14. Lovera M, Astolfi A (2004) Spacecraft attitude control using magnetic actuators. *Automatica* 40: 1405–1414. https://doi.org/10.1016/j.automatica.2004.02.022

15. Servidia P, Sanchez Peña R (2005) Practical Stabilization in Attitude Thruster Control. *Ieee T Aero Elec Syst* 41.

16. Stoneking E (2018) 42: An Open-Source Simulation Tool for Study and Design of Spacecraft Attitude Control Systems. *NASA Document*. Available from: https://ntrs.nasa.gov/citations/20180000954.

17. McComas D, Melton R (2017) OpenSatKit Enables Quick Startup for CubeSat Missions, SSC17-II-1, *31st Annual AIAA/USU Conference on Small Satellites*, Logan, Utah.

18. Canepa V, Husain S, Servidia P (2024) Trade-Off Analysis for Attitude Control in Highly Elliptical Orbits. *IEEE ARGENCON 2024, San Nicolás*, Argentina. https://doi.org/10.1109/ARGENCON62399.2024.10735803

19. Ovchinnikov M Yu, Roldugin DS (2019) A survey on active magnetic attitude control algorithms for small satellites. *Prog Aerosp Sci* 109. https://doi.org/10.1016/j.paerosci.2019.05.006

20. Trégouët JF, Arzelier D, Peaucelle D, et al. (2013) Static input allocation for reaction wheels desaturation using magnetorquers, *19th IFAC Symposium on Automatic Control in Aerospace, IFAC Proceedings*, 46: 559–564. https://doi.org/10.3182/20130902-5-DE-2040.00066

21. McKeen P (2025) Computational Methods to Improve Satellite Attitude Determination and Control with a Focus on Autonomy, Generalizability, and Underactuation, *MIT Department of Aeronautics and Astronautics Thesis*. Available from: https://dspace.mit.edu/handle/1721.1/158874.

22. Zarourati M, Mirshams M, Tayefi M (2024) Active Underactuation Fault-Tolerant Backstepping Attitude Tracking Control of a Satellite with Interval Error Constraints. *Adv Control Appl Eng Ind Syst*. https://doi.org/10.1002/adc2.215

23. Horn RA, Johnson CR (2013) *Matrix Analysis*, Cambridge University Press.

24. Servidia P, Canepa V, Rizzo A, et al. (2024) Flight Safety, Guidance, Navigation and Control on a Suborbital Mission Concept with Aerobraking. *IAA Latin American Conference on Small Satellites, Technology and Applications*, Salta, Argentina.

25. Servidia P, Giribet J, España M (2024) Suborbital Ascent Guidance and Control on VEx1B. *IAA Latin American Conference on Small Satellites, Technology and Applications* Salta, Argentina.

26. Stack Exchange (2017) *Maximum angle between a vector x and its linear transformation Ax*. Available from: https://www.math.stackexchange.com/questions/2266057/maximum-angle-between-a-vector-x-and-its-linear-transformation-a-x.

27. Balan R (2005) An Extension of Barbashin-Krasovskii-LaSalle Theorem to a Class of Nonautonomous Systems. *Nonlinear Dynam Syst Theor* 8. https://doi.org/10.48550/arXiv.math/0506459
28. Hassan Khalil (2002) *Nonlinear systems*, Prentice Hall.
29. Della Rossa F, Bergamasco M, Lovera M (2012) Bifurcation analysis of the attitude dynamics for a magnetically controlled spacecraft, *2012 IEEE 51st IEEE Conference on Decision and Control (CDC)*, 1154–1159. https://doi.org/10.1109/CDC.2012.6426150
30. Ward MJ (2017) *Chapter 3: Basic Floquet Theory*. Available from: https://link.springer.com/content/pdf/10.1007/978-1-84800-911-0_3.pdf.
31. Liberzon D, *Switched Systems: Stability Analysis and Control Synthesis*, University of Illinois at Urbana-Champaign, Lecture Notes, Available from: https://liberzon.csl.illinois.edu/teaching/Liberzon-LectureNotes.pdf.
32. Hanisch E (2024) Numerical simulations of the attitude control of the USAT-I, *IAA Latin American Conference on Small Satellites, Technology and Applications*, Salta, Argentina.
33. Alonso R, Anigstein P, Sánchez Peña RS (1998) *SAC-A attitude control design*, AS 98-307, Spaceflight Dynamics.
34. Slotine JJ, Li W (1991) *Applied Nonlinear Control*, Prentice Hall.
35. CubeSpace, *CubeWheel*, 2025. https://www.cubespace.co.za/products/cubewheel
36. Moreno A, Canepa V, Giribet J, et al. Simulador GNSS para la Evaluación de Algoritmos de Navegación Intergada en Vehículos Aeroespaciales, *XI Congreso Argentino de Tecnología Espacial (CATE 2021)*, Mendoza, Argentina.
37. Burroni T, Servidia P (2022) Control Orbital Autónomo Restringido de Bajos Empujes y Filtrado de Elementos Orbitales *2022 IEEE Biennial Congress of Argentina (ARGENCON)* San Juan, Argentina. https://doi.org/10.1109/ARGENCON55245.2022.9939743
38. Burroni T, Thangavel K, Servidia P, et al. (2024) Distributed satellite system autonomous orbital control with recursive filtering. *Aerosp Sci Technol*. https://doi.org/10.1016/j.ast.2023.108859

Appendix

Here we describe briefly the parameter specifications for the USAT-I simulation using the 42 simulator. The simulation input specification file *Inp_Sim.txt* defines the simulation times, names of auxiliary files (orbit, spacecraft, etc), environment, and celestial bodies of interest. In particular, it was configured to consider the disturbance torques due to aerodynamic, gravity gradient, solar radiation pressure, and residual magnetic dipole effects.

In the spacecraft specification file, named *SC_USAT1.txt* and provided as an auxiliary file, the reaction wheel is defined as follows:

```
************************** Wheel Parameters ***************************
FALSE                         ! Wheel Drag Active
FALSE                         ! Wheel Jitter Active
1                             ! Number of wheels
============================  Wheel 0  ================================
0.0                           ! Initial Momentum, N-m-sec
```

```
0.0    0.0    1.0                 ! Wheel Axis Components, [X, Y, Z]
0.23e-3 1.77e-3                   ! Max Torque (N-m), Momentum (N-m-sec)
2.1128e-6                         ! Wheel Rotor Inertia, kg-m^2
0                                 ! Body
0                                 ! Node
NONE                              ! Jitter Input File Name
...
```

where the wheel’s drag is not active as we have included it explicitly.

The three MTBs are specified on each axis as follows:

```
*************************** MTB Parameters ***************************
3                                 ! Number of MTBs
==============================  MTB 0  ================================
0.24                              ! Saturation (A-m^2)
1.0    0.0    0.0                 ! MTB Axis Components, [X, Y, Z]
0                                 ! Flex Node Index
...
```

There are six coarse Sun sensors (CSSs), located one per face, described as follows:

```
********************** Coarse Sun Sensor ******************************
6                                 ! Number of Coarse Sun Sensors
============================== CSS 0 ==================================
1.0                               ! Sample Time,sec
1.0   0.0   0.0                   ! Axis expressed in Body Frame
90.0                              ! Half-cone Angle, deg
1.0                               ! Scale Factor
0.001                             ! Quantization
0                                 ! Body
0                                 ! Node
...
```

Finally, the three-axis magnetometer is specified per axis as follows:

```
*************************** Magnetometer *****************************
3                                 ! Number of Magnetometer Axes
============================== Axis 0 =================================
1.0                               ! Sample Time,sec
1.0   0.0   0.0                   ! Axis expressed in Body Frame
800.0E-6                          ! Saturation, Tesla
0.0                               ! Scale Factor Error, ppm
13.0E-9                           ! Quantization, Tesla
13.0E-9                           ! Noise, Tesla RMS
0                                 ! Node
...
```

The spacecraft body is composed as given in the following paragraph:

```
*********************************************************************
*********************** Body Parameters *****************************
*********************************************************************
1                                 ! Number of Bodies
================================ Body 0 ============================
3.086                             ! Mass
0.031   0.031   0.007             ! Moments of Inertia (kg-m^2)
0.0   0.0   0.0                   ! Products of Inertia (xy,xz,yz)
0.0003   -0.0012   0.004          ! Location of mass center, m
0.0   0.0   0.0                   ! Constant Embedded Momentum (Nms)
0.00048   0.00048   0.0           ! Constant Embedded Magnetic Dipole (A-m^2)
USAT1.obj                         ! Geometry Input File Name
```

```
NONE                          ! Node File Name
NONE                          ! Flex File Name
...
```

The initial attitude and velocity are also specified in the same file.

Finally, the orbit parameters are specified in a separate file, named *Orb_LEO_USAT1.txt* and provided as an auxiliary file, as follows [32]:

```
<<<<<<<<<<<<<<<<<  42: Orbit Description File   >>>>>>>>>>>>>>>>>
Low Earth Orbit               !  Description
CENTRAL                       !  Orbit Type (ZERO, FLIGHT, CENTRAL, THREE_BODY)
::::::::::::::  Use these lines if ZERO          :::::::::::::::::
MINORBODY_2                   !  World
FALSE                         ! Use Polyhedron Gravity
::::::::::::::  Use these lines if FLIGHT        :::::::::::::::::
0                             !  Region Number
FALSE                         ! Use Polyhedron Gravity
::::::::::::::  Use these lines if CENTRAL       :::::::::::::::::
EARTH                         !  Orbit Center
TRUE                          !  Secular Orbit Drift Due to J2
KEP                           !  Use Keplerian elements (KEP) or (RV) or FILE
PA                            !  Use Peri/Apoapsis (PA) or min alt/ecc (AE)
600.0  600.0                  !  Periapsis & Apoapsis Altitude, km
600.0  0.0011                 !  Min Altitude (km), Eccentricity
97.77                         !  Inclination (deg)
0.0                           !  Right Ascension of Ascending Node (deg)
0.0                           !  Argument of Periapsis (deg)
0.0                           !  True Anomaly (deg)
6978.0 0.0 0.0                !  RV Initial Position (km)
0.0  7.56  0.0                !  RV Initial Velocity (km/sec)
TRV                           !  TLE, TRV, or SPLINE file format
"TRV.txt"                     !  File name
"EXAMPLE 1"                   !  Label to find in TLE or TRV file
:::::::::::::  Use these lines if THREE_BODY     ::::::::::::::::
...
******************  Formation Frame Parameters  ***********************
...
```